

# A Tensegrity Joint for Low-Inertia, Compact, and Compliant Soft Manipulators

Yifeng Hao, Xiaomei Wang, Xiaoqi Song, Yingqi Li, Henry Fu, Alex Pui-Wai Lee, Kenneth Man-Chee Cheung, James Lam, and Ka-Wai Kwok\*

Compact, low-inertia, and soft compliant robotic joint mechanisms are in great demand for ensuring safe interactions in human–robot collaborative tasks. Tensegrity, of which the structural integrity is constrained by tension, does not involve static/sliding friction among the rigid components. However, this mechanical stability is very susceptible to actuation errors. It requires complex kinematics modeling and sophisticated control model with sensing feedback. Herein, a low-inertia tensegrity joint that is covered/protected by a fiber Bragg grating (FBG)-embedded silicone sheath is proposed, with the aim to reinforce the joint motion stability and enable self-contained sensing feedback. A learning-based closed-loop controller is also designed and trained with the proper joint configurations selected by a two-step sampling method. Both the kinematics and static equilibriums of such configurations can be well satisfied. The experiments demonstrate that the joint can follow paths accurately in 2D by compensating manipulation error shortly under the closed-loop control. The joint stiffness can also be varied against the external/impulsive disturbances. It can be foreseen that this primitive robot joint component with 2 degrees of freedom (DoFs) can provide safe, compliant interaction with human, for which a simple test of maneuvering a portable ultrasound probe ( $\approx 210$  g) for abdominal imaging is demonstrated.

properties due to the conventional rigid links and rotary joints that consist of a motor, brake, harmonic drive, or other gearbox. This leads to inherent actuation friction and high inertia, which can impart resistive forces during interactions and risks from instantaneous collisions even when the robot is under back-drivable control. Compact, low-inertia, and even soft compliant robotic joint mechanisms are in great demand for ensuring safe interactions, thus also avoiding cumbersome set-ups due to the separation between human and robot.

Tendon-driven robots, which enable remote transmission to reduce robot link size and weight while maintaining sufficient distal dexterity and force,<sup>[5]</sup> have drawn increasing interest. Many emerging applications include serial-link manipulators,<sup>[6]</sup> exoskeletons,<sup>[7]</sup> and surgical instruments such as endoscopes,<sup>[8]</sup> cardiac catheters,<sup>[9]</sup> and robotic drills.<sup>[10]</sup> The structural stiffness can be increased with preloading of the tendons. However, in particular for serial-link or soft continuum


robots, such preloading would induce substantial axial compression on the backbone links and contact joints, giving rise to increased overall bending stiffness and friction, thereby requiring larger pulling forces to drive the robot motion in return.

In contrast, tensional integrity, namely, tensegrity, which consists of rigid bodies (struts) and tendons, is constrained by the tensions in the system, while there is no direct contact between the rigid components. Thus, no sliding or static friction is

## 1. Introduction

Collaborative robots have been widely applied across a variety of fields, such as industrial manufacturing<sup>[1,2]</sup> and robotic-assisted surgeries,<sup>[3,4]</sup> for the purpose of reducing repeatable work while assisting human with physical effort and facilitating precise motion. However, current collaborative robotic systems usually implement bulky robot arms with poor haptic and ergonomic

Y. Hao, X. Wang, X. Song, Y. Li, J. Lam, K.-W. Kwok  
Department of Mechanical Engineering  
The University of Hong Kong  
Hong Kong 999077, P. R. China  
E-mail: kwokkw@hku.hk

 The ORCID identification number(s) for the author(s) of this article can be found under <https://doi.org/10.1002/aisy.202300079>.

© 2023 The Authors. Advanced Intelligent Systems published by Wiley-VCH GmbH. This is an open access article under the terms of the Creative Commons Attribution License, which permits use, distribution and reproduction in any medium, provided the original work is properly cited.

DOI: 10.1002/aisy.202300079

H. Fu, K. M.-C. Cheung  
Department of Orthopedics and Traumatology  
The University of Hong Kong  
Hong Kong 999077, P. R. China

A. P.-W. Lee  
Department of Medicine and Therapeutics  
The Chinese University of Hong Kong  
Hong Kong 999077, P. R. China

K. M.-C. Cheung  
Department of Spinal Surgery  
The University of Hong Kong-Shenzhen Hospital  
Shenzhen 518053, P. R. China

involved among rigid bodies. External forces will be passively distributed through a network of tension, but not breaking the static equilibrium. Structural stiffness of this tensegrity would be solely determined by the tensions. However, this mechanism would also allow significantly less tolerance to any errors of actuation, as a result of complex kinematics modeling and the sophisticated actuation sensing required. Therefore, tensegrity structures were mostly found in various locomotion robots capable of rolling,<sup>[11]</sup> pipe crawling,<sup>[12]</sup> and swimming,<sup>[13]</sup> and soft continuum or serial-link robot architectures aiming entire body shape control like compliant grasping,<sup>[14–16]</sup> accredited to the high power density and flexibility of tensegrity, but were rarely implemented on the robots targeting dexterous end-effector manipulation.

To take full use of tensegrity's promising characteristics, the modeling and control of such an overconstrained mechanism must be advanced. It is worth noting that both kinematics and static equilibrium constraints have to be well satisfied. This is known as the form-finding problem,<sup>[17]</sup> for which force density method (FDM)<sup>[14,17,18]</sup> was commonly used to simplify the robot as a cable network comprising nodes, bars, and cables, but which would be oversimplified and limited to specific mass interstructures. Finite element modeling was also used to linearize tensegrity dynamics model,<sup>[19]</sup> but which would be too computationally intensive. To bypass such intensive computation, Real2Sim2Real<sup>[20]</sup> strategy was proposed to employ differentiable physics engine for simulating the robot kinematics/dynamics model based on the limited data observed from the real robot. The resultant simulated model can offer sufficient training datasets to form a deep-learning model for real use. In such simulated physics engines, the prestress, material, and geometric information could be taken into account for deducing the nonlinear equilibrium equations.<sup>[21]</sup>

Therefore, sufficiency of sensing data, regarding the robot configuration feedback, is of importance to the aforementioned data-driven approaches. Encoding the tendons length is a common approach to reflect the robot configuration through its forward kinematics, if existing. Johnson *et al.* used stretchable tendon sensors<sup>[22]</sup> to detect the morphology of a crawling tensegrity robot with the purpose of environment exploration.<sup>[23,24]</sup> Similarly, Booth *et al.*<sup>[25]</sup> used many strain sensors to estimate the shape of a rolling tensegrity robot. To extend the application to serial-link or soft compliant manipulators<sup>[18,26,27]</sup> and grippers,<sup>[14]</sup> which have to support and experience a great variety of external loads in task space, the overall robot control performance should be improved by the inherent robot stiffness varying in a wide range, rather than just heavily relying on promising sensing feedback of the robot configuration.

Among the studies about tensegrity structures, only a few of them are on serial-link robots. Taking inspiration from human anatomical structures, a tensegrity manipulator with two joints that functioned similarly to human elbow and shoulder was developed, incorporating actuation tendons to lift its lower segments. This represents the early implementation of translating static tensegrity structure into an actuated robotic manipulator.<sup>[28]</sup> Stacked mechanisms are commonly used to construct tensegrity manipulators from several similar segments, in which each segment was supported by tendons linked to the apex of its lower segment.<sup>[14,18,29]</sup> Due to the lack of accurate kinematics model and sensing approach, there were spared tendon lengths

that did not fully constrain the structure but the tendons were only passively straightened by the gravity load, to avoid structural collapse from actuation errors. These underconstrained mechanisms would be susceptible to small variations of external loads, causing the manipulation behavior to be inconsistent over different times of operation, resulting in great challenges when implementing data-driven control approaches. To enhance the manipulation repeatability, elastic springs have been adopted to replace the tendons,<sup>[30]</sup> hence, suppressing the free motions of the manipulator. The bending motions became controllable through the use of trained mapping between the desired bending curvatures and their corresponding tendon configurations.<sup>[15]</sup> Thin McKibben artificial muscles composed of inner pneumatic bladders and exterior braided sleeves were also used as actuation tendons to enhance the impact resistance.<sup>[16]</sup> However, the compliance induced by springs or artificial muscles would deteriorate control accuracy, particularly when supporting a varying load. A variable stiffness mechanism was developed to adjust the bending stiffness of a tensegrity spine,<sup>[31]</sup> which allowed each segment to be rigidly attached to its adjacent segments through a spherical pin when pulling all the tendons, but at the expense of reduced workspace in this stiffer state. Mimicking the anatomical structure and kinematics of the human knee, a bioinspired robotic knee was developed with adjustable joint stiffness, achieved by tightening/releasing the springs connected to the tendons, while the joint provided only one passive degree of freedom (DoF) and was actuated by an external connecting bar.<sup>[32]</sup> Another stiffer tensegrity manipulator actuated by pneumatic cylinders was also designed,<sup>[33,34]</sup> but its bulky and heavy robot links result in limited operation bandwidth ( $\approx 1$  Hz). Furthermore, the sole use of tendon length encoding in the existing tensegrity manipulators would make the robot configuration sensing feedback very unreliable. Possible tendon slack usually caused by the modeling/actuation errors would worsen sensing feedback, thus giving incorrect cues about the robot end-effector pose.

To this end, we propose a compact, low-inertia, and soft tensegrity robot joint capable of enabling safe interaction and robustness to disturbance. Such a joint can also be incorporated with a high-level data-driven controller and closed-loop sensing feedback of optical fiber Bragg grating (FBG)-based shape sensing. These FBGs can detect sparse strain changes of the soft robot body, allowing real-time shape sensing of continuum robots<sup>[35,36]</sup> and soft skins<sup>[37]</sup> with large deformation, accredited to its high sampling rate ( $\geq 100$  Hz) and dense strain measurements with a single connection of an optical fiber. In our previous work, FBGs helically wrapped on the soft robot surface enabled sensitive shape feedback for reliable closed-loop control.<sup>[38,39]</sup> In this study, a stretchable silicone sheath embedded with FBGs was integrated as a soft skin protecting our proposed compact tensegrity joint. A learning-based controller with the joint shape feedback and tendon length encoding was constructed. A two-step sampling approach is proposed to ensure the joint manipulation under kinematics and static equilibrium. The major contributions of this work are concluded as follows: 1) Study of a fully constrained tension-actuated soft robotic joint featuring actuation redundancy for varying the 2-DoF joint configuration as well as joint stiffness; its precise motion control with variable stiffness has not yet been reported. 2) Incorporation with FBG-based soft sensing feedback for self-contained

closed-loop control of the joint kinematics and its actuation stability. 3) Design of a learning-based control model trained by a two-step sampling approach, for which experimental validation on the joint actuation accuracy and compliance, as well as robustness to the load and disturbance, is also conducted.

## 2. Results and Discussion

A tensegrity joint prototype was proposed, of which the main body is 61 mm long with an outer diameter of 56 mm and a weight of about 60 g, comprising two 3D-printed circular frames made of resin. The joint integrity is maintained by four braided steel tendons (OD $\varnothing$ 1.2 mm) (Figure 1a) preloaded. Note that the tension of the central tendon always compensates the preloaded pulling forces of the other three actuation tendons (Figure 1b). By adjusting the differences among these three tendon lengths, the upper frame can be steered in 2 DoFs, pan/tilt, swinging about the apex of the lower frame (Figure 1c), thereby generating bending motions of the joint. While satisfying both the kinematics and static equilibriums, respectively, coordinating the length differences and tensions of the three tendons, such a joint configuration can be stabilized firmly to support external load.

A prestretched silicone (Ecoflex30, Smooth-On Inc., USA) sheath was wrapped on the cylindrical surface between the upper and lower frames, not only with the aim to enhance the bending motion stability, but also to restore the joint to its natural

configuration. To sense the configuration change, apart from measuring the tendon lengths encoded by the motors, deformation along the silicone rubber sheath can also be strong cues of how the joint is being bent. Therefore, an optical fiber with a single-core FBGs (FBGS International) is embedded and wounded helically around the silicone sheath, so as to reflect the sparse strain changes along with the joint bending. In our experimental validations, as shown in Figure 2a, we clamped the joint horizontally so as to afford the most gravity load or external force disturbance to be applied on the links or end-effector. The distal tip (end-effector) was positioned by 150 mm ( $\approx$ 250% self-height) from the upper frame along a rigid rod. Its pose could be tracked by an electromagnetic (EM) tracking system (NDI Medical Aurora) as the ground truth. With this 150 mm arm length, we could analyze the joint manipulation and control performance in a proper spatial resolution, illustrating any error observed readily within the workspace.

### 2.1. End-Effector Workspace Analysis

The learning-based control implemented a two-step sampling strategy, aiming to ensure the system under both kinematic and static equilibriums of the tensegrity joint. Initial tendon length combinations, acting as the expected sampling of the joint configurations, were generated by a basic geometric model as formulated in Section 4. In this step, such preliminarily generated configuration does not guarantee that the joint is in static equilibrium and may induce tendon slacking, which would cause the joint to collapse. Up to the next step of sampled data adjustment, which is a one-go calibration, all the three tendons could be tightened without slacking based on the motor torque control feedback. A light torque threshold (0.15 N·m) was preset, so not to overtighten the tendons too much. The above two-step sampling method could ensure the valid tendon length combinations, namely, the actuation space, within which the joint would not collapse because of the tendon slacking. Throughout the two-step sampling process, the distal tip poses and the tendon configurations were recorded by the EM positional tracker and motor encoders, respectively. A neural network (NN) model was used to map the collected data between the actuation space and the task workspace, thus forming a joint controller for further use.

Figure 2b shows the workspace collected by the two-step sampled distal tip positions. Along the workspace, actuation efficiency is quantified at each sampled tip position, indicating the total amount of tendon length changes required to move the tip to its adjacent position by a unit of length. The less the total change of tendon lengths, the higher the quantified efficiency, which is used to evaluate the variation in actuation demand across the workspace. At each sampled position, four adjacent positions were randomly selected for the calculation of actuation efficiency, and such efficiency has been normalized between 0 and 1. The workspace projected on 2D circle with the diameter of 116 mm, corresponding to a bending angle of  $\pm 25^\circ$ . The pattern of the resultant actuation efficiency appears hexagonally symmetric. When the tip moves along the directions where the tendons were located, the joint pan angle aligns with that of all the tendons. This allows for the most efficient adjustment of the joint tilt angle, resulting in the formation of a hexagon

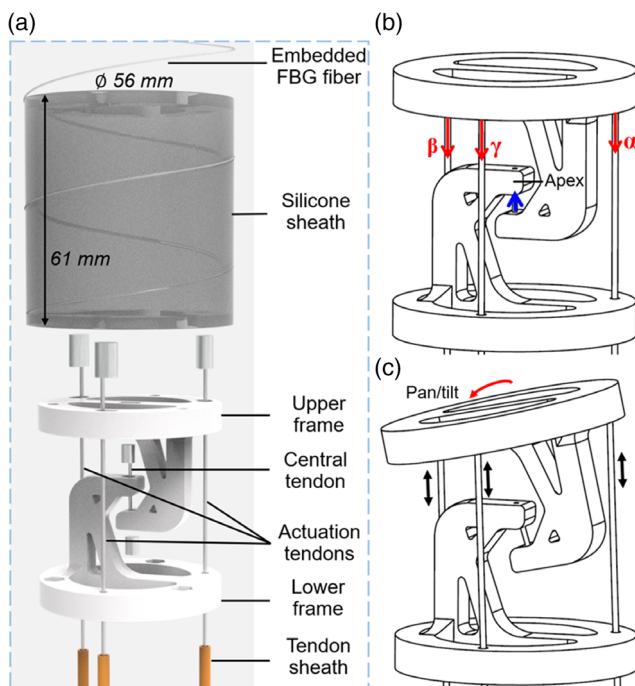


**Figure 1.** Tensegrity joint with FBG-empowered shape sensing. a) Interior structure of the tensegrity joint covered by a silicone sheath helically wrapped with an FBG optical fiber. b) Natural configuration with equal lengths of all three actuation tendon vectors  $\alpha$ ,  $\beta$ , and  $\gamma$ . c) Pan/tilt bending by adjusting tendon lengths. During static equilibrium, tension of the central tendon (linking the two apices) is always equal to the sum of the other three tendon tensions.

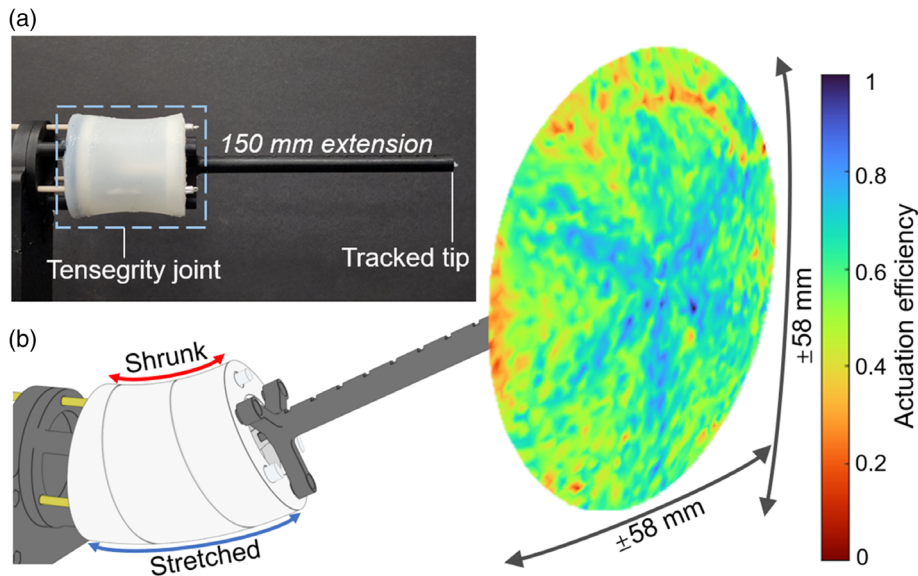


**Figure 2.** Experimental setup for evaluating the workspace of the distal tip and the control performance of the tensegrity joint. a) Experimental setup of the joint mounted with a 150 mm distal tip extension. b) 3D workspace of the distal tip measured by an EM tracker. Higher actuation efficiency (cooler color) indicates less actuation changes necessary for the same amount of tip displacement.

pattern due to the three tendons. Moreover, the actuation becomes less efficient when the tip moves close to the circular edge of the workspace, indicating the need for dramatic changes in tendon lengths at large bending angles. The range of available bending angles could be varied by adjusting the joint dimensions. Reducing the joint radius could increase the overall actuation efficiency, thus allowing larger bending angles. However, this would decrease the joint payload capacity due to the reduced moment arm, which in return requires a larger force output from the actuation system. Dynamic response of the tendon motors used is also the key to defining the proper range of bending angles, such that the tendon slacking can always be compensated sufficiently fast. This explains the angle  $\pm 25^\circ$  based on our choice of tendon motor (Dynamixel, MX-64AT). Furthermore, this choice also affects the optimal control bandwidth, for which we also conducted an experimental frequency response study. Two motors were commended to pull and release their tendons simultaneously. This pull-and-release is a harmonic motion repeated periodically at the input frequency ranged from 0.1 to 6 Hz. The distal tip motion tracked by the EM tracker becomes the output. **Figure 3a** is the resultant Bode plot, showing the tip motion magnitude decayed by 3 dB, when the pull-and-release was repeated at 4.5 Hz. For the sake of fair performance analysis of our proposed joint, in the latter experiments, we have kept the joint control commands or the joint motion changes below such an optimal bandwidth (4.5 Hz)

Path following test was carried out to evaluate the joint manipulation accuracy. Open-loop control was first applied, which solely employed the sampled actuation space to operate the joint (at  $< 4.5$  Hz) without any shape sensing feedback to the controller (see the Video SV1, Supporting Information). The distal tip was controlled to follow an “8”-like path within  $80 \times 40$  mm. As shown in **Figure 3b**, the tip motion was EM-tracked and projected on 2D for readily illustrating the path deviation (**Figure 3c**) in a unit of Euclidean distance. Root-mean-square error (RMSE) was

used to indicate overall accuracy of the path following task. Even under the open-loop control, this path following RMSE was measured as 1.10 mm only. This indicates the two-step sampling method, as well as the trained NN-based controller, can fully constrain the actuation space, ensuring zero tendon slacking throughout the path following task. However, to our observation, the motors used could somehow be coordinated poorly, not well in sync, due to the serial interfacing between the computer and the electronic motor drivers. Although the actuation has been within the sampled space, the control discrepancy among the three motors would still deteriorate this open-loop control performance, causing the sudden deviation plotted in **Figure 3c**. It is expected that closed-loop control with higher level sensing feedback of joint configuration/shape would minimize the path deviation further.

## 2.2. FBG-Based Sensing Feedback Control

Light wavelength shifted by FBG is proportional to the change of strain applied on the FBG. Together with all the sparse FBG-strain change data collected via a single-core optical fiber, we could have enough cues for estimating the joint configuration in pan/tilt DoFs (**Figure 4a**), accredited to the unique mapping from the combination of detected FBG-strains to the joint configuration. To construct this mapping, real-time FBG-strains were collected as the input training dataset, while the EM-tracked configurations were captured as the output training dataset during a calibration movement of the joint. It is worth noting that the EM tracking was only used in the calibration for sensing and control models training, and also as the ground truth or baseline for our performance analysis. We propose to train the two models, namely, the FBG shape sensing and the controller, by using the EM-tracked joint configuration as the feedback. Regarding the shape sensing, a single-layer NN model incorporates input as

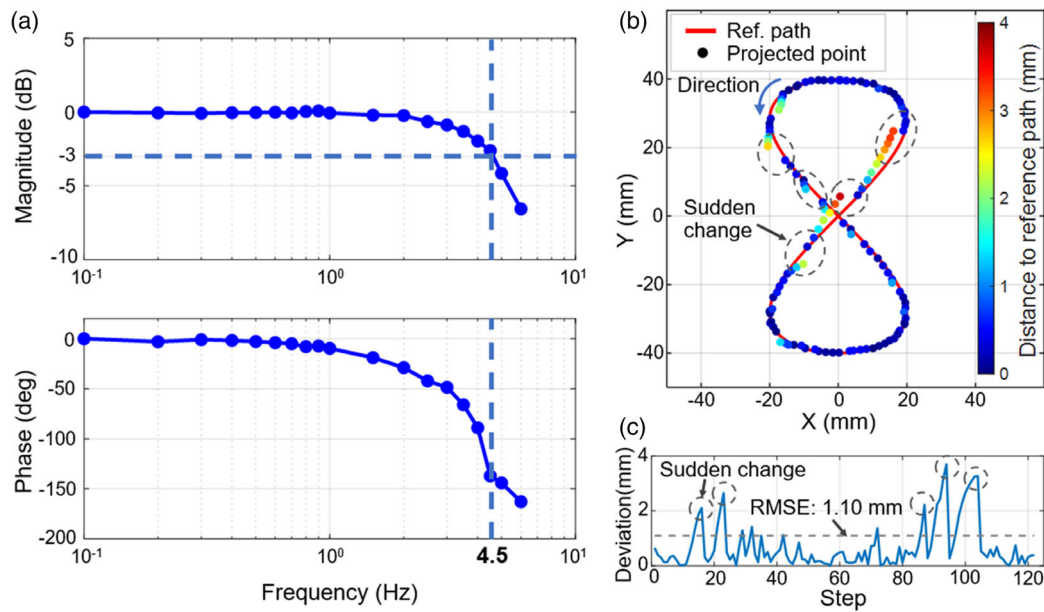


**Figure 3.** Experimental frequency response and “8”-like path following performance under open-loop control. a) Cutoff frequency measured at 4.5 Hz. b) 2D-projected reference and actual paths. c) Corresponding tracking deviation calculated as Euclidean distance bounded below 4 mm throughout the cycle of 121 time steps ( $\approx 30$  s).

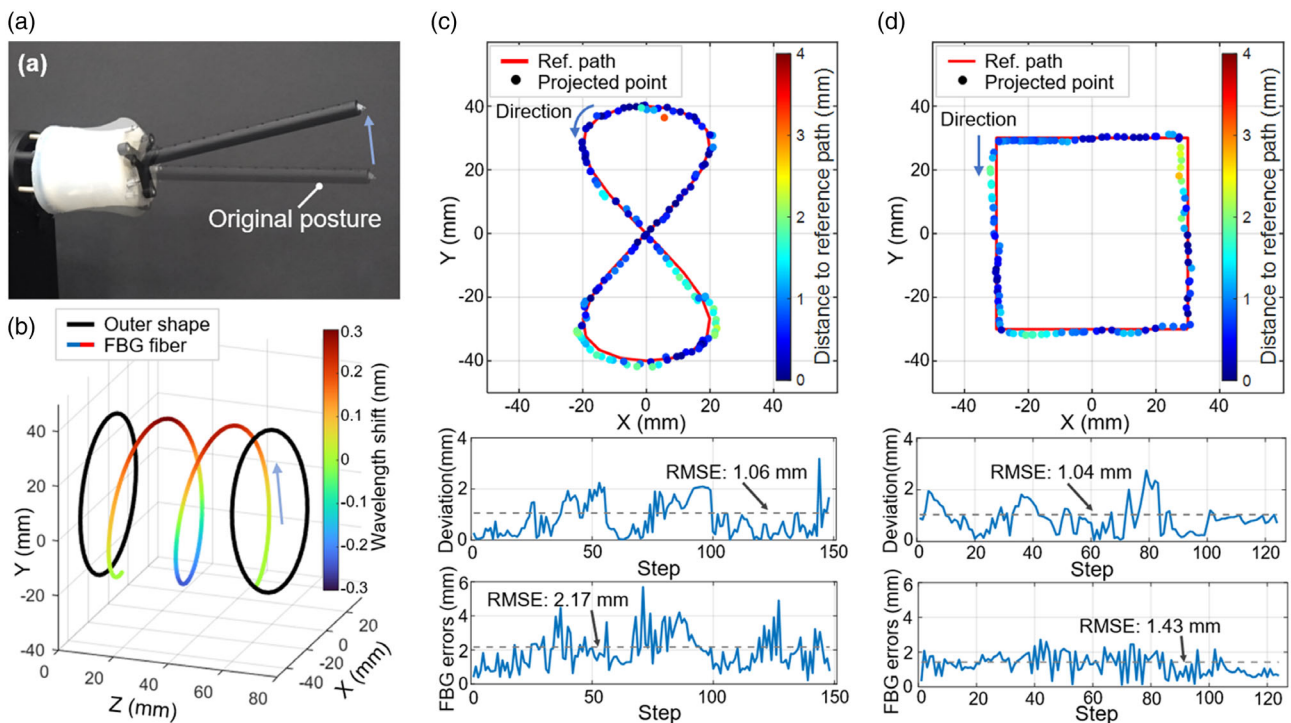


**Figure 4.** Path following with learning-based control and FBG-based shape sensing feedback. a) Upward bending of the tensegrity joint showing the half-range of the path following motion. b) Plot of 18 FBG wavelength shifts overlaid along the helical layout of the optical fiber embedded inside the joint’s sheath. Pan/tilt motion of the joint shape reconstructed based on a trained NN model can also be observed as shown in the Video SV2, Supporting Information. Similar to Figure 3b,c, the tracking deviation under closed-loop control with the FBGs is demonstrated in path following tasks for c) an “8”-like path and d) square path.

real-time FBGs strain data, and output as the corresponding joint configuration. During the data acquisition for training, the joint

was commanded to move along a spiral path within the workspace (Figure 2b), and samples were collected each time after

the tracked tip moved with a preset distance. The closed-loop controller was trained using another single-layer NN model during the two-step sampling. A large amount (10 000) of paired joint configurations were collected such that the tip separation of the paired has to be less than a preset step size. This formed the input training dataset of joint motions in multiple directions. The corresponding actuation changes acted as the output training dataset. Thus, the trained model could correct deviations of the joint motion by using the sensing feedback. With the FBG-strain data and the shape sensing model, the joint configuration can be reconstructed in real time; as can be seen in Figure 4b and Video SV2, Supporting Information, the helical layout of FBG optical fiber moved along with the 2-DoF joint motion estimated. In our future work with a serial manipulator formed by the presented joints, this will also facilitate motion planning with sufficient knowledge of the robot surrounding.<sup>[40]</sup>

Here, we propose to use the embedded FBG fiber as a self-contained positional sensor and also use it for closed-loop control. The path following tests with the same “8”-like pattern (Figure 4c) as in the open-loop control task, as well as the square path (Figure 4d), were carried out to evaluate the closed-loop control accuracy with FBG sensing feedback. The tip motion was EM-tracked and projected on 2D, and the sensing errors were calculated by the Euclidean distance between the EM-tracked and FBG-predicted tip positions. Although compared to the open-

loop control (RMSE of 1.10 mm), the RMSE under closed-loop control (1.06 mm) was only slightly lower, the sudden deviation (e.g., marked in Figure 3b) reduced significantly (Figure 4c). Only 6.8% and 5.6% of the deviations are above 2 mm in the “8”-like and square paths, respectively, showing closed-loop motions is smoother, relative to 11.5% deviations that is above 2 mm under the open-loop control. Moreover, the peak deviation is reduced by 13.9% in the “8” path. For the FBG sensing errors, the 2.17 mm RMSE (Figure 4c) corresponds to an angular error  $<1^\circ$ . The positional deviations sensed by FBG were fed into the controller, enabling real-time correction, and compensating for the incoordination of the motor actuations observed in the open-loop control.

To evaluate joint manipulation accuracy under external loads, path-following task under high load was performed without preloading the tendons. The same paths as in Figure 4c,d were used but an additional 114 g load was placed on the joint link which was 35 mm far from the joint upper frame (see the Video SV2, Supporting Information). It is worth noting that no retraining or recalibration was conducted for the learning-based controller, that is, only the samples without external load were involved in the training data. Two cases were tested to evaluate the manipulation robustness, one with the load from the beginning and consistently throughout the path following (Figure 5a), and the other was applied with the load intermediately (Figure 5b).

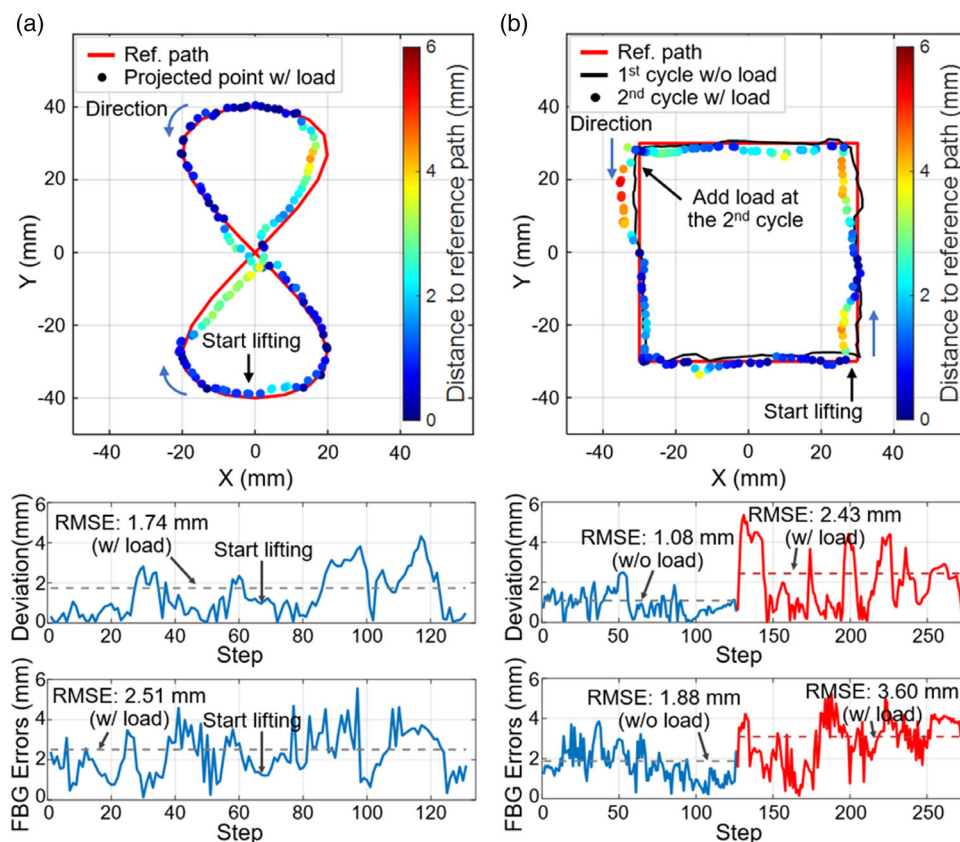


**Figure 5.** Two cases of path following with a load of 114 g (about twice the self-weight) and no tendon preload. a) In the first case, consistent load was applied throughout path following of the “8”-like path. b) In the second case, the robot ran without external load in the first cycle while the load was applied at the beginning of the second cycle without pauses.

In the case with the load applied from the beginning, the tensegrity joint maintained low tracking deviations with an RMSE of 1.74 mm. The robot followed the target path closely when moving downward, while larger deviations were observed during the lifting motion (marked by warmer color in Figure 5a). This may be mainly caused by the FBG-based sensing error when encountering untrained deformations of joint sheath. Such error occurs when large tension incremented to support a stronger load. Therefore, the external load applied on the end-effector also stretches the joint sheath and results in strain changes along the FBG fiber, sequentially degrading the position predictions used as the control feedback. This prediction or sensing errors were further increased when the external load was added intermediately. In this case, deviations were significantly increased in the first few seconds when the impulsive disturbance (i.e., adding the load) was applied. Although the joint could approach toward the target path again, the deviations were still 39.7% larger than those in the case with the load from the beginning. As the robot was horizontally clamped, all the tendons took the most effort from the load gravity, causing the joint upper frame shifted from its original configuration. This stretches the sheath further on one side, causing the strain change distribution slightly different from that in the unloaded configurations during the data training. In the case with the load from the beginning, the load-induced stretching was already involved when the robot started moving. However, when the load was added intermediately, this additional stretching change resulted in an uneven distribution of overall strain changes. Therefore, tightening the tendons with stronger preloading can increase the structural stiffness, hence reducing the uneven sheath stretching along its cylindrical surface, eventually, would reduce the sensing error. The synergetic use of FBGs with another type of self-contained sensors, such as inertial measurement units (IMUs) that could feedback with promising joint orientation, thus enhancing the joint control performance, would be studied in our future work.

### 2.3. Joint Dynamics and Compliance Performance

It is hypothesized that the proposed joint enables variable stiffness by adjusting the preload on tendons. Reducing the preload would result in higher compliance, but also makes the joint softer. The joint stiffness under three levels of tendon preload, 3, 5, and 10 N, was evaluated in two tests, respectively, with static load and impulsive disturbance. In the load-deflection test, static loads ranging from 100 to 500 g were sequentially applied 10 mm aside from the joint upper frame. The test was repeated 3 times for each preloading level and load condition, during which the tip deflection under each load was measured by the EM tracker, and shown in Figure 6a. In the test with 500 g load, the tip deflection was reduced by 19.5% and 35.1%, respectively, under 5 and 10 N preloading, compared to the deflection of 9.32 mm under 3 N preloading. Similar results were also found in the impulsive disturbance test, where the force disturbances were applied by dropping a 114 g weight from 1 cm above the link which is 35 mm far from the joint upper frame, and the test was repeated 5 times for each preloading level (Figure 6b). Relative to the average peak deflection of 13.63 mm when 3 N preload applied, there was deflection reduced by 35.3% and 75.8%, respectively, under 5

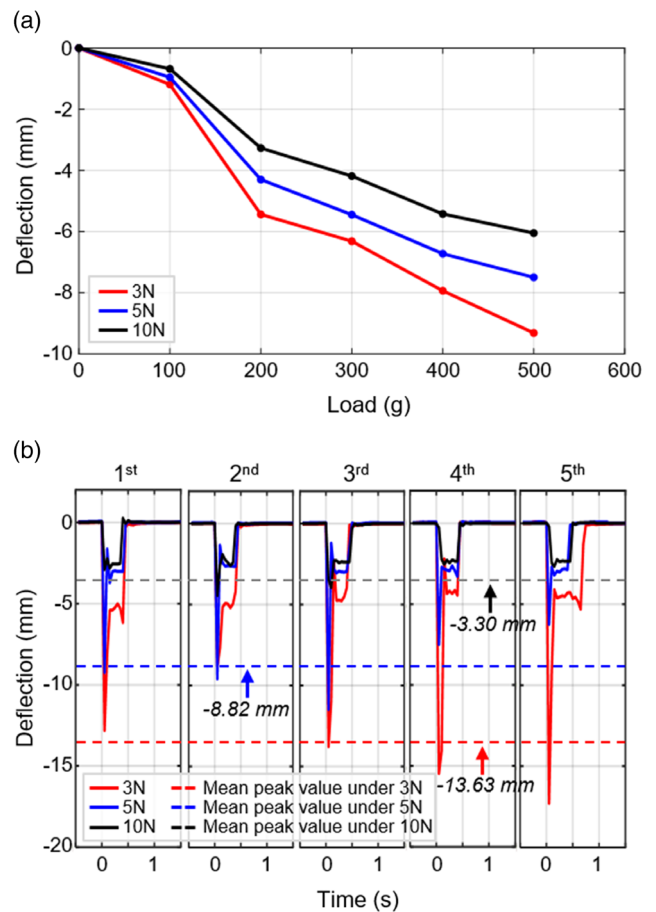


**Figure 6.** Three levels of joint stiffness applied by the tendon preloading with 3, 5, and 10 N. a) Varying loads were applied 10 mm aside from the joint upper frame. The tip deflection under each load was recorded. b) To generate an impulsive disturbance, a 114 g weight was dropped from 1 cm above onto the joint link. This impulsive disturbance test was repeated 5 times for each preloading level.

and 10 N preloading. The less deflection indicates the increased joint stiffness, according well with our hypothesis, such that the structural tensegrity stiffness is controllable by varying the tendon preloads. It is also worth noting that for impulsive disturbance, the joint under all these preloading levels could restore its natural configure in the similar amount of time, 0.5 s, indicating the robust response or resistance to external disturbances. It can be explained by the fully constrained property of our presented tensegrity. In addition to the preloading, the two joint frames were wrapped by a prestretched elastic (silicone) sheath. This also possesses inherent compliance to any force interaction on the joint body and link.

To further explore the dynamic performance, a 360 g can of cola was held 45 mm aside from the joint upper frame (Figure 7a). It was lifted (up and down, Figure 7b) and shaken (left and right, Figure 7c) at an average speed of 5.41 and 6.79 cm s<sup>-1</sup> (angular speed of 0.95 and 1.19 rad s<sup>-1</sup>), respectively, also with rapid change of motion directions (see Video SV1, Supporting Information). Note that the can weighs 6 times the tensegrity joint itself. The motion outcome was smooth,

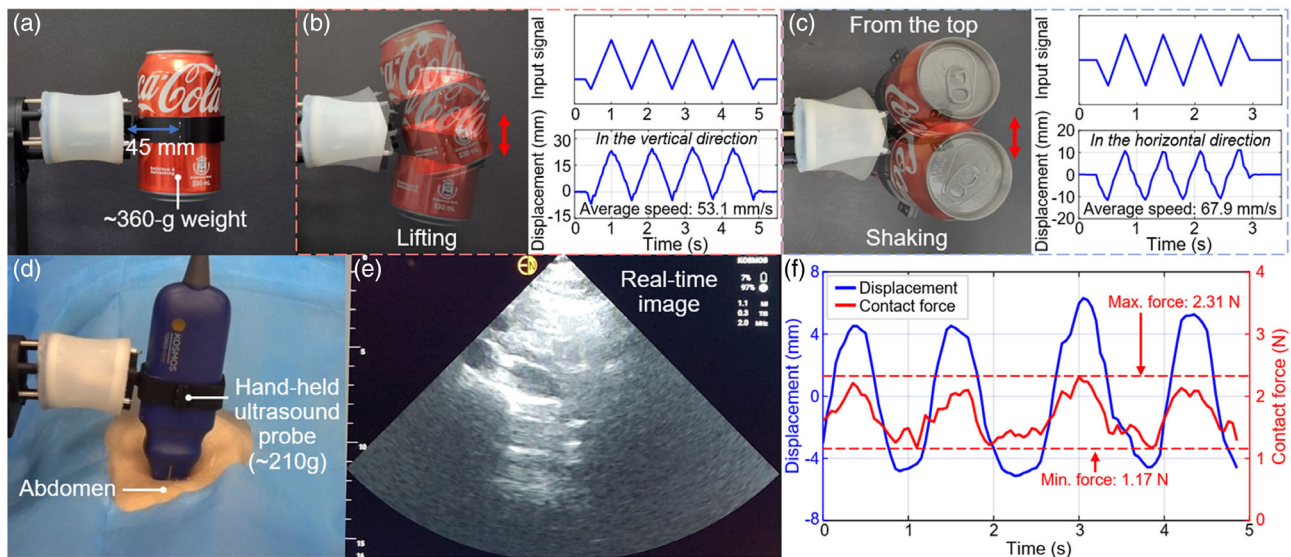


**Figure 7.** a) Manipulation of a coke can, which is 6 times the joint self-weight. The can was lifted b) and shaken c), with rapid change of motion directions. d) Maneuvering a portable ultrasound probe for abdominal imaging. The probe is about 3.5 times the joint self-weight. e) Corresponding ultrasound image captured under the compliant joint motion. f) The passive motion of the ultrasound probe that complied with breathing, when low joint stiffness was applied. The contact force between the ultrasound probe and abdomen skin was maintained within a certain range.

accredited to no static or sliding contact friction between the two joint frames. The fully constrained property and low inertia of the joint enable a maximum angular acceleration of over  $10 \text{ rad s}^{-2}$ , giving rise to agile and flexible manipulation without overshoot. With the controllable stiffness and compliance of the joint, the tensegrity joint has great potential to perform various tasks of interactions with human body. As shown in Figure 7d, we took ultrasound probe manipulation as an example, in which the joint was used to maneuver a  $\approx 210 \text{ g}$  portable probe (Torso-One, KOSMOS, USA) for abdominal ultrasound imaging (Figure 7e). The low joint stiffness applied could allow the probe to comply with any physiological motion mostly due to breathing. During the up-and-down probe displacement of about  $\pm 5 \text{ mm}$ , the contact force between the probe and the abdomen skin was kept within the range of 1.17–2.31 N (Figure 7f), thus maintaining the imaging quality. By adjusting the tensions, it could be controlled stiffer to conform the imaging on a region of interest. This joint dynamic property would add much confidence to telemanipulation of various ultrasound examinations.

### 3. Conclusion

This article proposed a compact, low-inertia, and reduced friction soft tensegrity robot joint with 2 DoFs, which would be considered a primitive component for the use in serial-link manipulator. The joint structural integrity can be maintained by four tendons, without involving sliding friction as seen in rotary joints even under high robot load and tendon pretensions. A soft skin sensor, which is an FBG-embedded silicone sheath, was designed to tightly wrap around the joint to enhance the structural stability, and also to provide self-contained shape sensing feedback. We also developed an NN-based data-driven controller, for which a

two-step sampling method was proposed to resolve the typical control challenge in meeting both the kinematics and static-equilibrium constraints requirements simultaneously, which is in great demand when requiring steady control of similar tensegrity structures. In the first step of sampling, initial actuation sequences were generated by a basic geometric model. In the next step, for each sampled kinematics configuration, the actuated tensions were adjusted online during the actual manipulation, thus compensating the error induced by modeling uncertainties. As a result, this further ensures static equilibrium of the actual samples. This method could maintain the quality of sampled data “learned” well by the controller. Therefore, the proper learning-based controller would eventually avoid any sudden collapse of the joint due to its tendons slacking as found in many similar kinds of tensegrity mechanisms.

Provided with just a preliminary implementation of simple servo motors to drive the tendons, we lowered the joint operation bandwidth below 4.5 Hz upon our test of frequency response. Together with the motor servoing of tendons length and the proposed shape sensing based on 18 FBGs of a single-core fiber, the tensegrity joint could follow prescribed paths along “8”-like and square patterns, respectively, with RMSE of 1.06 and 1.04 mm. Without preloading the tendons, the joint could still resist external disturbances, such as a 114 g load that is twice the joint weight, during the path following task. The precise motion control of similar tensegrity-based joints has not yet been reported.

A 360 g load (six times the self-weight) can be lifted and shaken by the joint. When holding a portable probe ( $\approx 210 \text{ g}$ ), ultrasound scanning can be performed with passive motions following the patient’s respiration and controllable motions to adjust the scanning pressure. Accredited to the actuation redundancy, the joint stiffness can also be varied by tendons preloading such that the joint deflection due to the impulsive external force



disturbance could be reduced by 35.3% and 75.8% when the three actuation tendons have been preloaded with 5 and 10 N, respectively (relative to 3 N preloaded setting). These key experimental validation results, along with the advantageous features of this proposed tensegrity joint, demonstrate its wide range of applications, in particular for scenarios requiring close and safe interaction with human, such as robotic ultrasound screening (Figure 7d,e) of patients, or joint replacement surgery (arthroplasty) where the surgeon has to manually handle the robotic manipulator (e.g., Mako SmartRobotics) end-effector under collaborative compliance control.

In this light of joint prototype, we foresee the manipulation accuracy and compliance control can be further improved by fusing new sensing modalities, e.g., IMUs, able to detect the joint pose in real time. High-end servo motors with precise tension control of tendons will be another prerequisite to realizing back-drivable manipulation. The joint dimensions can be scaled up/down to meet the requirements of the application scenario, while the maximum bending angle is primarily determined by the actuation performance of its tendon motors. A higher radius-to-length ratio of the joint could further increase its payload capacity. The inner space of the joint could be utilized as a working channel for end-effectors and additional sensors. When employing the joints in serial-link manipulators, the variable stiffness property could facilitate the decoupling of joint motions. However, the presented tensegrity design is susceptible to torsional disturbances; this could deteriorate the steady control of such manipulators, as the proximal joints may be subject to substantial torsional loads. Therefore, in the future work, torsional rigidity and stability of the joint will have to be reinforced and enhanced so as to fulfill various robot manipulation requirements. This new type of tendon-driven manipulator comprising the proposed 2-DoF tensegrity joints would become an alternative to conventional manipulator linked by rotary joints, each of which just provides 1-DoF rotation only. Considering the challenges of tendon management and motion decoupling among the joints, we will explore the use and design of advanced controllers, e.g., reinforcement-learning-based controllers,<sup>[41]</sup> so as to enhance the compliance variation and back-drivability of the resultant tensegrity manipulator, rather than just a single joint.

#### 4. Experimental Section

In this section, we explain the detailed structure of the proposed tensegrity joint. Formulation of the basic geometric model used to predefine possible sampled robot configurations is also detailed. A sampling approach, acting as a one-go calibration, which resolves typical control challenges of tensegrity, as well as the learning-based controller with FBG-based shape sensing feedback, is also introduced here.

**Tensegrity Robot Joint:** As shown in Figure 1b, the tensegrity joint mainly comprises two circular frames which were 3D-printed with high Young's modulus and lightweight UV-curable resin. These two frames had to be hinged by four braided steel tendons (ODØ1.2 mm), including three actuation tendons pulled by three motors beyond the joint structure, and one central tendon in balance of the three tendon pulling forces. Attributing to the tendon-driven mechanism that enables remote transmission, all the motors could be based and fixed on the ground. Note that the "L"-shaped struts of the two frames overlaid at a certain level allow a large bending angle ( $\pm 25^\circ$ ). The central tendon would afford high tension counteracting the high load manipulation; therefore, the struts and the tendon

connection points have to be made of very rigid and strong materials. The interior structure is rather simple, but the outer protection, namely, the rubber sheath (made of silicone, i.e., Ecoflex30, Smooth-On Inc.), is another crucial component. As the wrapped sheath is prestretched, its elasticity allows it to keep pulling the upper frame toward the lower one, ensuring the integrity by not just heavily relying on the three actuation tendon tensions. This also provides resistance to torsional force, and helps restore the joint to its original or natural equilibrium. Based on our previous implementations of FBG-based shape sensing,<sup>[38,39]</sup> an optical fiber with a single core of 18 FBGs (FBGS International) was helically wrapped inside the shallow groove on the soft sheath and sealed using silicone adhesive (Sil-Poxy, Smooth-On Inc.). It functions as a high-level sensor capable of sensing the joint configurations in real time ( $\geq 100$  Hz) for closed-loop feedback control. To demonstrate a certain level of high-power density performance, we prefer to design the joint in smaller form factors, with ODØ56 mm, 61 mm long and a weight of just about 60 g, including the 35 g silicone sheath.

**Basic Geometric Model:** To formulate the tensegrity joint kinematics for establishing its controller, the complex motion of the joint was first elaborated. As shown in Figure 8a, the central tendon ( $\overrightarrow{PQ}$ ) involves motions denoted by polar angle  $\theta$  and azimuth angle  $\varphi$ , both are rotated about the apex of the lower frame (point P), making the point Q lies in a spherical surface  $\mathbf{S}_Q := \{(Q_x, Q_y, Q_z) \mid |\overrightarrow{PQ}| = m\}$ , where  $m$  is the central tendon length. Simultaneously, the joint upper frame could rotate about Q and around its horizontal arm ( $\overrightarrow{QM}$ ), respectively, by angles  $\lambda$  and  $\sigma$ . Thus, the distal end of the joint, regarded as point E, lies in a set  $\mathbf{S}_E$

$$\mathbf{S}_E := \{(E_x, E_y, E_z) \mid |\overrightarrow{EQ}| = n, \overrightarrow{EQ} \cdot \overrightarrow{QM} = 0, M \in \mathbf{S}_M, Q \in \mathbf{S}_Q\} \quad (1)$$

where  $\mathbf{S}_M := \{(M_x, M_y, M_z) \mid |\overrightarrow{QM}| = r, Q \in \mathbf{S}_Q\}$  is a set of circles with center points following the movements of point Q;  $n = |\overrightarrow{A_uM}|$  and  $r = |\overrightarrow{EA_u}|$ , respectively, are the height and the radius of the upper frame. Note that the tensegrity structure is fully constrained by the actuation tendons; the actual task space  $\mathbf{S}_T$  is a subset of  $\mathbf{S}_E$  that satisfies the boundary conditions decided by static equilibriums. The angles,  $\lambda$  and  $\sigma$ , are both dependent on the angles,  $\theta$  and  $\varphi$ . This task space  $\mathbf{S}_T$  formed from the complex motions of the upper frame is not a spherical surface, unlike the typical rotary/universal joints (Figure 8b). With the presence of the aforementioned geometry constraints, analysis of the statics equilibriums usually involves singular matrices, making it very difficult to formulate a closed-form of the mapping between the task space  $\mathbf{S}_T$  and the corresponding tendon actuation configurations ( $\mathbf{q} = [|\alpha|, |\beta|, |\gamma|]^T$ ). Though numerical constrained optimization methods such as the force density method<sup>[42]</sup> and dynamic relaxation<sup>[43]</sup> have been proposed to deduce this mapping, determining the initial configurations for effective optimization is still an open problem. Therefore, we intend to apply data-driven methods to learn the joint kinematics, for which a basic geometric model was devised to initiate possible tendon configurations for sampling and model training.

The basic geometric model is deduced based on two assumptions: 1) there is no axial rotation of the central tendon in the absence of external disturbance; 2) the central tendon is always perpendicular to the upper frame so that angles  $\lambda$  and  $\sigma$  are set and not changed, as it is designed to be short for less overlap between the two frames. Thus,  $\overrightarrow{QM}$  is always perpendicular to  $\overrightarrow{PQ}$  and parallel to the plane containing points P,  $A_u$ , and O. Actuation tendon vectors  $\alpha$ ,  $\beta$ , and  $\gamma$  can be expressed as follows

$$\alpha = \frac{n-m}{m} \overrightarrow{PQ} - \overrightarrow{QM} - \overrightarrow{OP} - \overrightarrow{A_uO} \quad (2)$$

$$\beta = \frac{n-m}{m} \overrightarrow{PQ} - \overrightarrow{EB_u} - \overrightarrow{OP} - \overrightarrow{B_uO} \quad (3)$$

$$\gamma = \frac{n-m}{m} \overrightarrow{PQ} - \overrightarrow{EC_u} - \overrightarrow{OP} - \overrightarrow{C_uO} \quad (4)$$

Given the angles  $\theta$  and  $\varphi$ , the actuation lengths and vectors can be solved by

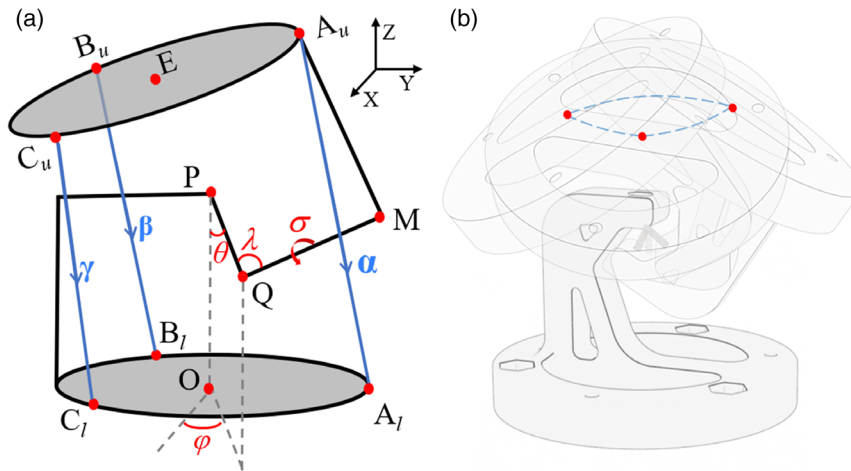


**Figure 8.** a) Key geometric parameters defined to deduce the joint kinematics. Four angles,  $\theta$ ,  $\varphi$ ,  $\lambda$  and  $\sigma$ , determine the joint configuration, but angles  $\lambda$  and  $\sigma$  are actually dependent on  $\theta$ ,  $\varphi$ , as a result of the 2 DoFs in the joint. b) Three possible joint configurations. Note that the end-effector positions (in red) form a task space that is not a spherical surface as found in typical rotary joints. It is generated by a rather complex swinging motion of the upper frame about the apex, P, of the lower frame.

$$\begin{cases} \alpha_x = (n - m)\sin\theta\cos\varphi \\ \alpha_y = (n - m)\sin\theta\sin\varphi - \frac{r\cos\theta}{\psi} + r \\ \alpha_z = (m - n)\cos\theta - \frac{r\sin\theta\sin\varphi}{\psi} - n \end{cases} \quad (5)$$

$$\begin{cases} \beta_x = (n - m)\sin\theta\cos\varphi + \frac{\sqrt{3}r(\psi - 1)}{2} \\ \beta_y = (n - m)\sin\theta\sin\varphi - \frac{r(\sqrt{3}\sin^2\theta\sin\varphi\cos\varphi - \cos\theta)}{2\psi} - \frac{r}{2} \\ \beta_z = (m - n)\cos\theta + \frac{r\sin\theta(\sin\varphi + \sqrt{3}\cos\varphi\cos\theta)}{2\psi} - n \end{cases} \quad (6)$$

where  $\psi = (\cos^2\theta + \sin^2\theta\sin^2\varphi)^{\frac{1}{2}}$ . Note that, up to this point, angles,  $\lambda$  and  $\sigma$ , are not yet solved to form a complete kinematics of the presented joint. A learning-based numerical approach is needed.

**Learning-Based Control:** As the tensegrity (inverse) kinematics is complicated by non-closed-form correlation between the task space ( $\mathbf{S}_T$ ) and the tendon actuation space ( $\mathbf{q}$ ), we intend to employ data-driven

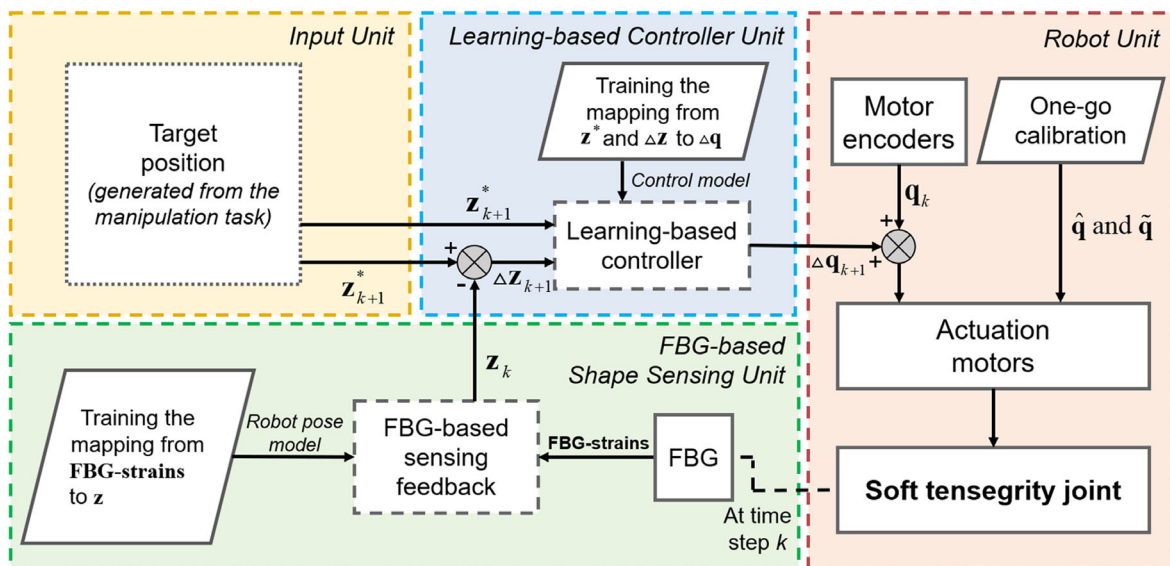


**Figure 9.** Proposed control schematic. Joint actuation space,  $\mathbf{q}$ , and tracked tip position,  $\mathbf{z}$ , are two key parameters covering all the units for robot sensing, control and actuation.

approaches capable of learning the analytical kinematics, as well as the control model based on sensing feedback. This approach outcome has to be supported by a large amount of high-quality sampled data for the learning. A two-step sampling approach based on the basic geometric model (Section 4) is proposed. In the first step of sampling, an actuation sequence containing initial tendon configurations was generated by the basic geometric (BG) model, such that  $\mathbf{q}_i = [|\boldsymbol{\alpha}_i|, |\boldsymbol{\beta}_i|, |\boldsymbol{\gamma}_i|]^T = \text{BG}(\theta_i, \varphi_i)$ , where  $i \in \{1, 2, \dots, N\}$  is the sample index,  $N$  is the total number of samples and the input angles variation as  $\theta_i \in [0, 25^\circ]$  and  $\varphi_i \in [0, 360^\circ]$ . Up to the second step, during the actual joint movement, all the actuation sequence has to be executed, in which the tendon combinations could be corrected in a torque-control manner by multiple trials of releasing ( $\tilde{\mathbf{q}}$ ) and pulling ( $\hat{\mathbf{q}}$ ) the tendon individually. Till all the three tendons tightened properly below the maximum motor torque threshold preset, the structure was ensured in static equilibrium, and then the task space sample, namely, the tracked tip position, and its actual configuration sample, which is the tendon length, were both recorded as a training dataset. Once  $N$  datasets are collected, an NN model with one hidden layer of 100 neurons is implemented to train controllers. The activation of *tanh* was exploited in the data training. The used L2 loss could be denoted by

$$\text{Loss} = \frac{1}{N} \sum_{i=1}^N \|\mathbf{q}_i^G - \mathbf{q}_i^P\|^2 \quad (8)$$

where  $\mathbf{q}_i^G$  and  $\mathbf{q}_i^P$  are the ground truth and the prediction of actuation configuration, respectively.

For the training of open-loop controller,  $N = 2237$  pairs of 2D tracked tip positions ( $\mathbf{z}$ ) and the corresponding tendon configurations ( $\mathbf{q}$ ) were regarded as input and output, respectively. For the training of closed-loop controller, position pairs, in which the tip separations were less than a preset step size, were searched randomly at first, forming a dataset (10 000 samples) of joint motions in various directions. Then these relative positional changes ( $\Delta\mathbf{z}$ ), together with their target positions ( $\mathbf{z}^*$ ), were taken as input. And the relative changes in tendon lengths ( $\Delta\mathbf{q}$ ) for each motion were taken as output.

Regarding the sensing feedback, it is required to create the mapping between FBG-strains and tip positions, for which we also adopted a data-driven approach. The joint was commanded to move along a spiral path within the workspace, during which the FBG-strains and the EM-tracked tip positions recorded were regarded as input and output, respectively. An NN model with one hidden layer of 100 neurons was utilized for training using 1275 samples. The schematic diagram of the proposed learning-based control method is shown in **Figure 9**.

## Supporting Information

Supporting Information is available from the Wiley Online Library or from the author.

## Acknowledgements

Research in this article was supported by the Research Grants Council (RGC) of Hong Kong (grant nos. 17205919, 17207020, 17209021, and T42-409/18-R), and the Innovation and Technology Commission (ITC) (MRP/029/20X) of the HKSAR Government under the InnoHK initiative, Hong Kong, via Multi-Scale Medical Robotics Center Limited and Centre for Garment Production Limited.

## Conflict of Interest

The authors declare no conflict of interest.

## Data Availability Statement

Research data are not shared.

## Keywords

fiber Bragg grating (FBG), learning-based control, soft manipulator, tensegrity, variable stiffness

Received: February 8, 2023

Revised: April 20, 2023

Published online:

- [1] B. Yao, Z. Zhou, L. Wang, W. Xu, Q. Liu, A. Liu, *Rob. Comput. Integr. Manuf.* **2018**, *51*, 158.
- [2] W. Wang, R. Li, Y. Chen, Z. M. Diekel, Y. Jia, *IEEE Trans. Autom. Sci. Eng.* **2019**, *16*, 640.
- [3] J. Chan, T. S. Auld, W. J. Long, S. Kreuzer, V. Campanelli, R. Liebelt, Y. D. Kissin, *Surg. Technol. Int.* **2020**, *37*, 299.
- [4] C. Batailler, D. Hannouche, F. Benazzo, S. Parratte, *Arch. Orthop. Trauma Surg.* **2021**, *141*, 2049.
- [5] H. M. Le, T. N. Do, S. J. Phee, *Sens. Actuators, A* **2016**, *247*, 323.
- [6] A. K. Mishra, E. Del Dottore, A. Sadeghi, A. Mondini, B. Mazzolai, *Front. Robot. AI* **2017**, *4*, 4.
- [7] T. Lee, I. Kim, Y. S. Baek, *Actuators* **2021**, *10*, 9.
- [8] T. Kato, I. Okumura, S. E. Song, A. J. Golby, N. Hata, *IEEE/ASME Trans. Mechatron.* **2015**, *20*, 2252.
- [9] D. B. Camarillo, C. F. Milne, C. R. Carlson, M. R. Zinn, J. K. Salisbury, *IEEE Trans. Rob.* **2008**, *24*, 1262.
- [10] Y. Wang, H. W. Yip, H. Zheng, H. Lin, R. H. Taylor, K. W. S. Au, *IEEE/ASME Trans. Mechatron.* **2021**, *26*, 1858.
- [11] M. Vespignani, J. M. Friesen, V. SunSpiral, J. Bruce, presented at 2018 *IEEE/RSJ Int. Conf. Intelligent Robots and Systems (IROS)*, IEEE, Piscataway, NJ, October 2018, <https://doi.org/10.1109/iros.2018.8594374>.
- [12] Y. Liu, X. Dai, Z. Wang, Q. Bi, R. Song, J. Zhao, Y. Li, *IEEE Rob. Autom. Lett.* **2022**, *7*, 11553.
- [13] B. Chen, H. Jiang, *Soft Rob.* **2019**, *6*, 520.
- [14] Y. Liu, Q. Bi, Y. Li, presented at 2021 *IEEE/RSJ Int. Conf. Intelligent Robots and Systems (IROS)*, IEEE, Piscataway, NJ, September–October 2021, <https://doi.org/10.1109/iros51168.2021.9635929>.
- [15] J. Zhang, Y. G. Hu, Y. Li, K. Ma, Y. J. Wei, J. Z. Yang, Z. G. Wu, H. Rajabi, H. J. Peng, J. N. Wu, *Adv. Intell. Syst* **2022**, *4*, 2200263.
- [16] W. Y. Li, H. Nabae, G. Endo, K. Suzumori, *IEEE Rob. Autom. Lett.* **2020**, *5*, 4345.
- [17] A. P. Sabelhaus, A. H. Li, K. A. Sover, J. R. Madden, A. R. Barkan, A. K. Agogino, A. M. Agogino, *IEEE Rob. Autom. Lett.* **2020**, *5*, 3982.
- [18] V. Ramadoss, K. Sagar, M. S. Ikbali, J. H. L. Calles, R. Siddaraboina, M. Zoppi, presented at 2022 *IEEE 5th Int. Conf. Soft Robotics (RoboSoft)*, IEEE, Piscataway, NJ, April 2022, <https://doi.org/10.1109/robosoft54090.2022.9762130>.
- [19] S. Ma, M. Chen, R. E. Skelton, *Compos. Struct.* **2022**, *280*, 114838.
- [20] K. Wang, W. R. Johnson III, S. Lu, X. Huang, J. Booth, R. Kramer-Bottiglio, M. Aanjaneya, K. Bekris, *arXiv* **2022**, *2209*, 06261.
- [21] S. Ma, M. Chen, Z. Peng, X. Yuan, R. E. Skelton, *Eng. Struct.* **2022**, *266*, 114618.
- [22] W. R. Johnson, A. Agrawala, X. Huang, J. Booth, R. Kramer-Bottiglio, presented at 2022 *IEEE Sensors*, IEEE, Piscataway, NJ,

- October–November 2022, <https://doi.org/10.1109/SENSOR52175.2022.9967136>.
- [23] W. Y. Li, A. Takata, H. Nabae, G. Endo, K. Suzumori, *IEEE Rob. Autom. Lett.* **2021**, *6*, 6228.
- [24] R. Kobayashi, H. Nabae, G. Endo, K. Suzumori, *IEEE Rob. Autom. Lett.* **2022**, *7*, 5349.
- [25] J. W. Booth, O. Cyr-Choiniere, J. C. Case, D. Shah, M. C. Yuen, R. Kramer-Bottiglio, *Soft Rob.* **2021**, *8*, 531.
- [26] H. C. Fu, J. D. L. Ho, K. H. Lee, Y. C. Hu, S. K. W. Au, K. J. Cho, K. Y. Sze, K. W. Kwok, *Soft Rob.* **2020**, *7*, 44.
- [27] J. D. L. Ho, K.-H. Lee, W. L. Tang, K.-M. Hui, K. Althoefer, J. Lam, K.-W. Kwok, *Adv. Rob.* **2018**, *32*, 1168.
- [28] S. Lessard, D. Castro, W. Asper, S. D. Chopra, L. B. Baltaxe-Admony, M. Teodorescu, V. SunSpiral, A. Agogino, presented at *2016 IEEE/RSJ Int. Conf. Intelligent Robots and Systems (IROS)*, IEEE, Piscataway, NJ, October 2016, <https://doi.org/10.1109/iros.2016.7759811>.
- [29] D. Zappetti, Y. Sun, M. Gevers, S. Mintchev, D. Floreano, *Adv. Intell. Syst* **2022**, *4*, 2200025.
- [30] J. Zhang, Z. Y. Kan, Y. Li, Z. G. Wu, J. N. Wu, H. J. Peng, *IEEE Rob. Autom. Lett.* **2022**, *7*, 6163.
- [31] D. Zappetti, R. Arandes, E. Ajanic, D. Floreano, *Smart Mater. Struct.* **2020**, *29*, 075013.
- [32] W. Liang, W. Wu, W. Chen, L. Ren, K. Y. Wang, Z. H. Qian, L. Q. Ren, *Bioinspiration Biomimetics* **2022**, *17*, 066006.
- [33] S. Ikemoto, K. Tsukamoto, Y. Yoshimitsu, *Front. Robot. AI* **2021**, *8*, 774253.
- [34] Y. Yoshimitsu, K. Tsukamoto, S. Ikemoto, presented at *2022 IEEE/RSJ Int. Conf. Intelligent Robots and Systems (IROS)*, IEEE, Piscataway, NJ, October 2022, <https://doi.org/10.1109/iros47612.2022.9982208>.
- [35] S. C. Ryu, P. E. Dupont, presented at *2014 IEEE Int. Conf. Robotics and Automation (ICRA)*, IEEE, Piscataway, NJ, May–June 2014, <https://doi.org/10.1109/icra.2014.6907368>.
- [36] K. Wang, J. D. L. Ho, X. Wang, G. Fang, B. Zhu, R. Xie, Y. H. Liu, K. W. S. Au, J. Y. K. Chan, K. W. Kwok, *IEEE Trans. Rob.* **2023**, *1*, <https://doi.org/10.1109/TRO.2023.3262118>.
- [37] K. Wang, C.-H. Mak, J. D. L. Ho, Z. Liu, K.-Y. Sze, K. K. Y. Wong, K. Althoefer, Y. Liu, T. Fukuda, K.-W. Kwok, *Adv. Intell. Syst* **2021**, *3*, 2100089.
- [38] X. Wang, G. Fang, K. Wang, X. Xie, K. H. Lee, J. D. L. Ho, W. L. Tang, J. Lam, K. W. Kwok, *IEEE Rob. Autom. Lett.* **2020**, *5*, 2161.
- [39] X. Wang, J. Dai, H. S. Tong, K. Wang, G. Fang, X. Xie, Y. H. Liu, K. W. S. Au, K. W. Kwok, *IEEE Trans. Rob.* **2023**, *1*, <https://doi.org/10.1109/tro.2023.3240556>.
- [40] K. W. Kwok, K. H. Tsoi, V. Vitiello, J. Clark, G. C. T. Chow, W. Luk, G. Z. Yang, *IEEE Trans. Rob.* **2013**, *29*, 15.
- [41] Y. Li, X. Wang, K. W. Kwok, presented at *2022 IEEE/RSJ Int. Conf. Intelligent Robots and Systems (IROS)*, IEEE, Piscataway, NJ, October 2022, <https://doi.org/10.1109/iros47612.2022.9981335>.
- [42] J. Y. Zhang, M. Ohsaki, *Int. J. Solids Struct.* **2006**, *43*, 5658.
- [43] N. B. H. Ali, L. Rhode-Barbarigos, I. F. C. Smith, *Int. J. Solids Struct.* **2011**, *48*, 637.